Published in *Medical Image Computing and Computer Assisted Intervention – MICCAI 2021*, 2021, part VI, pp. 451-460, which should be cited to refer to this work.
DOI : 10.1007/978-3-030-87231-1_44

Revisiting contour-driven and knowledge-based deformable models: application to 2D-3D proximal femur reconstruction from X-ray images

Christophe Chênes[1,2][0000-0001-8784-1467] and Jérôme Schmid[1][0000-0003-2464-8971]

[1] Dept. of Medical Radiology Technology, Geneva School of Health Sciences, HES-SO University of Applied Sciences and Arts of Western Switzerland
2 Medical Image Processing Lab, Institute of Bioengineering, School of Engineering, Ecole Polytechnique Fédérale de Lausanne
christophe.chenes@hesge.ch; jerome.schmid@hesge.ch

Abstract. In many clinical applications, 3D reconstruction of patient-specific structures is of major interest. Despite great effort put in 2D-3D reconstruction, gold standard bone reconstruction obtained by segmentation on CT images is still mostly used – at the expense of exposing patients to significant ionizing radiation and increased health costs. State-of-the-art 2D-3D reconstruction methods are based on non-rigid registration of digitally reconstructed radiographs (DRR) – aiming at full automation – but with varying accuracy often exceeding clinical requirements. Conversely, contour-based approaches can lead to accurate results but strongly depend on the quality of extracted contours and have been left aside in recent years. In this study, we revisit a patient-specific 2D-3D reconstruction method for the proximal femur based on contours, image cues, and knowledge-based deformable models. 3D statistical shape models were built using 199 CT scans from THA patients that were used to generate pairs of high fidelity DRRs. Convolutional neural networks were trained using the DRRs to investigate automatic contouring. Experiments were conducted on the DRRs, and calibrated radiographs of a pelvis phantom and volunteers – with an analysis of the quality of contouring and its automatization. Using manual contours and DRR, the best reconstruction error was 1.02 mm. With state-of-the-art results for 2D-3D reconstruction of the proximal femur, we highlighted the relevance and challenges of using contour-driven reconstruction to yield patient-specific models.

Keywords: 2D-3D X-ray reconstruction, Shape priors, Deformable Model.

1 Introduction and related work

3D reconstruction of patient-specific bone anatomy is of growing interest in many clinical applications, such as surgery planning, personalized implant design, and postoperative analysis [1], [2]. Focusing on total hip arthroplasty (THA), 3D reconstruction of the proximal femur enables better surgical planning and design of patient-specific surgical instruments – ultimately leading to more positive outcome for the patient. Today, gold standard reconstruction of bones is mainly obtained by segmentation on computed

tomography (CT) images [3] for planification purpose. However, this comes at the expense of exposing patients to significant ionizing radiation and increased health costs [1]. Alternatively, 2D-3D reconstruction offers a cost-efficient mean of obtaining patient 3D models from a few calibrated 2D X-ray images, while reducing ionizing dose.

2D-3D reconstruction tries to solve the challenging problem of recovering 3D information from partial 2D information. In orthopedic surgery, the shape and pose of 3D bony structures need to be recovered from single or multiple X-ray images [2]. If the 3D shape is known, 2D-3D reconstruction is equivalent to a rigid registration problem solved by optimization techniques [4]. Otherwise, shape and pose are estimated by non-rigid registration techniques often coupled with statistical models of shape and intensity appearance of the structures [5]. Most of these methods assume that X-ray imaging is calibrated[1] or implement a calibration procedure. Though it is the case in our study, we will not cover the calibration process – being out of the scope of this publication.

Non-rigid 2D-3D reconstruction approaches encode prior information about the 3D shape and appearance of the targeted structure in deformable models. These knowledge-based models can be manipulated to best fit the patient's target structure in the 2D images. Most approaches use a reference template of the structure features, whose variations are modeled by analytical [2], [6] but mostly statistical [5], [7]–[15] representations. To obtain patient-specific 3D reconstructions, deformable models are transformed using information inferred from X-ray images using two possible strategies: (a) correspondence of features or (b) simulated X-ray images. (a) tries to minimize the distance between features (e.g., contours) extracted on both the deformable model and the X-ray images – making the strategy particularly sensitive to the quality of extracted features [16]. (b) generates DRR from the deformable model and optimizes the image similarity between the DRR and X-ray images [5]. This strategy bypasses explicit feature extraction but is computationally time-consuming and usually requires close initialization.

Historically, 2D-3D reconstruction methods only took shape into account, using statistical shape models (SSMs). Since then, models including intensity or appearance – referred to as statistical shape and intensity models (SSIMs) – have been studied to include bone density. Lately, deep learning (DL) algorithms have also been applied to 2D-3D reconstruction of bones [17], [18].

In terms of reconstruction accuracy, state-of-the-art SSIMs methods yield reconstruction errors ranging from 1.18 to 4.24 mm [5]. A bone reconstruction error of 1 to 1.5 mm with successful registration in 95% of the time has been suggested as a good performance indicator [5], [19]. However, the maximum tolerated error depends on the target application, as e.g., this suggested maximum error can be excessive to design patient-specific implants and surgical instruments in case of THA. Lastly, comparison of bone reconstruction errors on different bony areas should be considered with care – the degree of superimposition of confounding structures in X-ray images being different (e.g., more challenging for the hip compared to the knee).

---

[1] Calibration parameters include e.g., source-detector distance, pixel size, central point, relative transformations between multiple images, etc.

These observations motivated us to revisit the development of a patient-specific 2D-3D reconstruction method for the proximal femur based on a novel combination of contours, image cues, and knowledge-based deformable models, with a focus on the detailed analysis of the quality of the contours, their impact on the reconstruction and their possible automation. Another contribution also lies in the preparation and evaluation of a high-quality synthetic dataset derived from a large number of real pathological cases of the hip joints prior to THA surgeries.

2 Method and material

In the following, we present our methodology with the processed datasets to train and evaluate our approach.

Statistical shape models. We collected 199 anonymized CT images of the hips from THA patients (aged 16 to 94, median 71 years) including gold-standard bone reconstructions performed semi-automatically by expert radiographers – resulting in 115 right and 84 left proximal femurs. Using R3DS Wrap software, we fit, for left or right, a same triangular mesh (left: 4585 vertices, right: 4626 vertices) of the proximal femur to the gold-standard reconstructions – yielding point correspondence across wrapped shapes. Using Generalized Procrustes similarity alignment, all shapes were co-aligned, and a subsampled version of each aligned shape was produced (1153 and 1156 vertices for left and right sides). Using Principal Components Analysis, left and right multiresolution SSMs were finally built using the fine and coarse resolutions [20]. In the following, the mean shapes of the SSMs will be denoted as the template shapes.

Contour definition. Image contours can be manually delineated, estimated by an automatic approach, or derived from a ground-truth. In any case, we consider contours as a collection of 2D pixel points. However, to inject knowledge and robustify the segmentation process, we also produce *mapped* contours. The idea is to associate groups of 3D vertices M_j of the template shape to specific subsets of contour points m_j – resulting in a 2D-3D mapping. For the proximal femur, we defined 6 groups corresponding to the femoral head and neck, the greater and lesser trochanters, and the intertrochanteric line and crest. To automatically derive contours, we used a state-of-the-art DL architecture, the U-Net++ model [21] that improves the established U-Net approach and that we coupled with a RegNetY encoder [22]. Contours were extracted as the boundaries of inferred segmentations.

Knowledge-based deformable model. Model reconstruction aims at deforming the template shapes using the calibrated X-ray images to recover the unknown femoral shape and pose with respect to the imaging system. Our approach follows the Newtonian dynamics-driven model deformation described in [20], in which a shape is deformed over time under the effect of forces applied to its vertices. Internal forces

enforce model smoothness, local compliance to the initial shape ("shape memory") and similarity to the closest shape generated from the corresponding SSM.

Image forces ensure meaningful deformation using image gradient and contours. Based on the calibrated geometry information, we can identify which shape vertex P_i contributes to salient image edges, known as the silhouette [23], and project them on the X-ray images as image positions p_i. Then, a sampling strategy in a neighborhood centered on p_i and directed by the projected mesh normal at P_i is used to probe image candidate positions r_i that maximize, gradient direction and magnitude [20] for the image force, and the proximity to contours for the contour force. If the contours are mapped, we only consider candidate positions mapped with the group of the corresponding 3D vertex P_i – preventing the incorrect attraction to confounding edges not easily distinguishable by gradient information. Image candidates in X-ray image I_k for gradient r_i^g and contour r_i^c forces are then back-projected as 3D lines $l_i^g = (O_k, r_i^g)$ and $l_i^c = (O_k, r_i^g)$, where O_k denotes the X-ray source position. Finally, gradient and contour forces are defined as spring forces attracting the vertex P_i to the closest points on lines l_i^g and l_i^c [20], with a parameter α weighting the force intensity.

3D landmarks are computed as the closest points to back-projected lines of 2D landmarks manually clicked in the images. By defining once the same landmarks on the template shapes, we can initialize the pose and global scale of the coarse shape in the calibrated geometry coordinate system by similarity alignment of corresponding 3D landmarks. In our case, landmarks were placed on the greater and lesser trochanters, and the center and fovea capitis of the femoral head.

Synthetic X-ray dataset. Since CT images were acquired and used for patient-specific THA planning, X-ray images were not included in the dataset. We thus generated for each patient a pair of high fidelity DRRs from their CT scan – using a DL approach able to model polychromatic X-ray spectra as well as stochastic noise and X-ray scattering [24]. We extended the approach to better model detector response and the effect of anti-scatter grids. All acquisition parameters were controlled, leading to a perfect calibration for the 398 synthetic images produced. AP and lateral (LAT) views at a relative 75° angle were computed with a focal length of 120 cm, a resolution of 3000x3000 px and a square pixel spacing of 0.15 mm. The simulated X-ray beam characteristics were: 2.5 mm Al filtration, 80 kV and 25 mAs (AP), and 90 kV and 40 mAs (LAT). An anti-scatter grid with a 16:1 ratio was modelled. Though DRRs are not perfect X-ray images, the adopted DL method produces more realistic results than simple ray-casting approaches. An example of data for one patient is shown in **Fig. 1**a&b. By projecting the silhouette of the reconstructed models onto the DRRs, high quality 2D contours were created for both views. Since we wrapped a template model for building the SSM, we could identify by closest distance the mapped regions on reconstructed models – leading to projected mapped contours. Initialization landmarks were also available in 3D segmented models and were projected similarly.

Real X-ray dataset. Real X-ray images were acquired for a pelvis phantom and three volunteers (3 healthy males, aged 32, 37 and 44). After duly filled informed consent, a

pair of calibrated X-ray images were shot for each volunteer in AP and LAT views (75° angle) in a clinical setup – using a designed protocol aiming at not disrupting the clinical routine, while including a calibration device, and a rotative platform for ensuring angle accuracy and minimal leg movement between the shots. Acquisition parameters were set to 120 cm, 70 kV (AP) and 75 kV (LAT) with automatic exposure control. Femoral bone models were derived from previous MRI acquisitions.

For the pelvis phantom – containing human bones – a CT scan and manual reconstruction of the bones were produced. Three AP/LAT acquisitions were performed in different setups with varying calibration device position and parameters settings. An example of AP X-ray image for the phantom is shown in **Fig. 1**c.

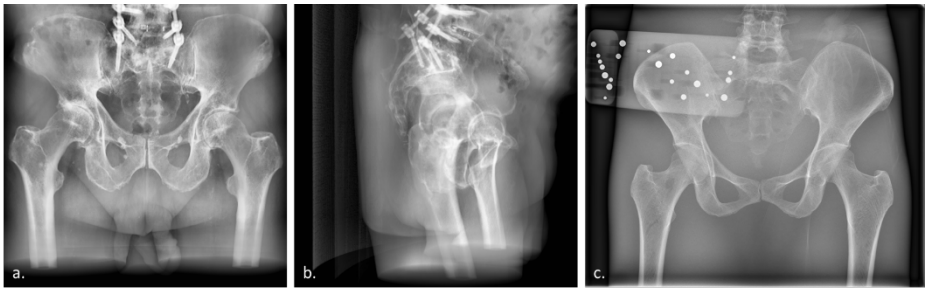

Fig. 1. Example of synthetic X-ray in AP (a.) and LAT (b.) views, and of real X-ray in AP view for the pelvis phantom (c.). The calibration device composed of metallic spheres can be spotted.

3 Results and discussion

Experiments for 2D-3D reconstruction of the proximal femur were conducted on both synthetic (DRRs) and real X-ray datasets. To thoroughly assess our method accuracy with different contouring strategies, we compared the use of reference contours vs automatically estimated contours, in presence or absence of mapped contours.

Evaluation metrics and implementation details. For the reconstruction metric, average absolute surface distance (ASD) was used and statistical significance between different strategy results were assessed using the two-sided Wilcoxon signed-rank test with a significance level of 0.01 – results not being normally distributed. Dice similarity coefficient (DSC) was used to assess the 2D image segmentation accuracy of the DL approach. In synthetic experiments, we used a leave-one-out strategy to train the SSMs, while a 10-fold cross-validation was chosen to evaluate the DL segmentation. An automatic image augmentation [25] was applied to enlarge the training dataset, and a 20-80% validation-training split was used for each fold.

Following [20], we empirically set the force parameters based on a fine-tuning with 3 randomly chosen DRR cases. Deformation took place during 3 stages with 500, 400 and 300 iterations respectively, during which the coarse shape resolution was used at the first stage, and the fine resolution for the remaining stages. Internal forces were weighted at each stage according to a specific schedule [20]: shape memory force $\alpha =$

$0.5; 0.1; 0.3$, SSM force $\alpha = 0.1; 0.4; 0.1$ and smoothing force $\alpha = 0.1$. For image forces, parameters were dependent on the use or not of DL-derived contours (**Table 1**).

Table 1. Parameters of image forces in experiments, s being in mm [20].

	Without DL-based contours						**With DL-based contours**					
	Gradient force			Contour force			Gradient force			Contour force		
stage	α	L	s	α	L	s	α	L	s	α	L	s
1	-	-	-	0.1	201	0.2	-	-	-	0.1	201	0.2
2	-	-	-	0.2	141	0.2	-	-	-	0.2	141	0.2
3	0.1	21	0.1	0.2	141	0.2	0.2	21	0.1	0.05	141	0.2

Tests were performed on a computer running under Windows 10 with an AMD Ryzen 5 3600 6-Core 3.6GHz processor and 32GB RAM. The deformable model was implemented in C++ while the U-Net++ approach used Python 3.9 and PyTorch 1.7.1.

Synthetic dataset results. On the large DRR dataset our 2D-3D reconstruction method was tested in optimal (perfect calibration and reference contours, as exemplified in **Fig. 2**a. in green) and automatic (DL method for extraction of contours) conditions. The higher complexity of LAT view prevented for this view the use of the DL approach. Hence, for experiments on automatic contours, AP contours were extracted with DL (e.g., **Fig. 2**a. in red) while reference LAT contours obtained by projection were used. In this case, the contours were not mapped.

Table 2. Mean ASD errors with standard deviations for the different contouring strategies tested on the synthetic dataset.

Reference contours		**Automatic contours**	
not mapped	mapped	not mapped	not mapped, gradient boost
1.16±1.01 mm	1.02±0.89 mm	1.98±1.89 mm	1.68±1.57 mm

Table 2 presents the results of our method applied on the synthetic dataset with reference and automatic contours. We obtained the best 3D reconstructions (ASD 1.02±0.89 mm) when using the mapped reference contours (e.g., **Fig. 2**b.&d.) – the most complete approach. The use of mapped contours improved reconstruction accuracy (p-value<$1e^{-12}$). Despite a satisfactory 2D DSC error of 0.957 (CI at 95%:[0.95,0.965]), automatic contours were less accurate and led to greater 3D ASD error, but still within the range of results of published works. To counterbalance the quality of the contours, our approach also takes advantage of image gradients. In the case of less accurate contours - as here for automatic contours - the gradient force should make it possible to catch up to a certain precision. To verify this, we repeated an experiment using the automatic contours with a "boosted" gradient by adding a gradient force at stage 2 ($\alpha = 0.1, L = 31, s = 0.5$) and by increasing the gradient force coverage at stage 3 ($s = 0.2$). These results (ASD 1.68±1.57 mm vs 1.98±1.89 mm, p-value<$1e^{-11}$) highlight the relevance of using image gradients to improve the robustness of the overall approach (cf., **Fig. 2**c.&e.). From the clinical THA point of view, the

highest reconstruction errors were located on the femoral head, which is of a lesser interest since it will be resected. The pathological "quality" of a random sample of 58 femurs (e.g., presence of several or severe osteophytes) was visually checked by 3 radiographers and classified into 3 balanced categories: "good" (19), "fair" (15) and "poor" (24). Our manual (mean ASD of 0.98, 1.03 and 0.96) and automatic (DSC of 0.96, 0.94 and 0.97) approaches appear to be robust to pathological variations.

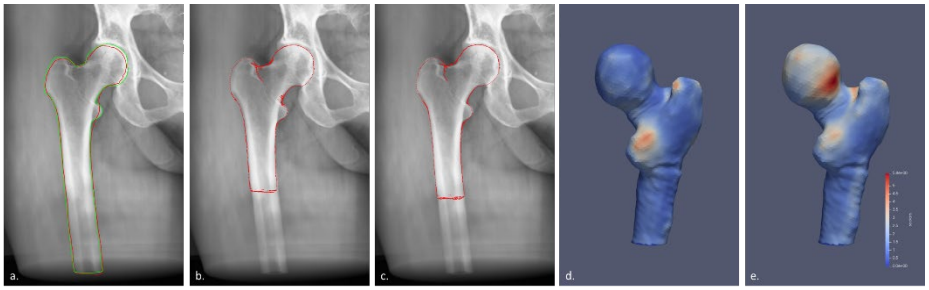

Fig. 2. Example of (a.) reference (in green) and DL-based (in red) input contours and the projection of their 3D reconstruction result silhouette in AP for (b.) reference contours and (c.) automatic contours. 3D models with mean ASD error for 115 right femurs are shown for (d.) mapped reference contours (ASD 1.06±0.97 mm) and (e.) automatic contours (ASD 1.63±1.53 mm).

Real X-ray dataset results. Our method has also been tested on six pairs of real X-ray images. First on the phantom data, then on the less controlled volunteers' data.

For the pelvis phantom, acquisitions were repeated three times with some variations of the attached calibration device (visible in **Fig. 1**c). Contours and landmarks were drawn manually. Results on the pelvis phantom for the different setups and with mapped and unmapped contours strategies are reported in **Table 3**. The mapping improved the results for setups 1 and 3 (p-value < $1e\text{-}^{16}$), while the difference was not statistically significative for setup 2 (p-value = 0.013).

Table 3. Mean ASD errors with standard deviations for the different setups and with and without mapped contours for the pelvis phantom real X-ray dataset

	Setup 1	**Setup 2**	**Setup 3**
not mapped	1.85 ± 1.65 mm	1.2 ± 1.03 mm	1.60 ± 1.39 mm
mapped	1.13 ± 1.18 mm	1.21 ± 1.21 mm	1.21 ± 1.23 mm

As for the phantom, the contours and landmarks were manually annotated for volunteers' data, and the impact of the contour mapping was analyzed. The results for mapped and not mapped contour strategies are displayed in **Table 4** for all three volunteers. Similarly, the mapping improved the results for volunteers 1 and 3 (p-value < $1e\text{-}^{15}$), but for volunteer 2 the difference was not significant (p-value = 0.013).

Table 4. Mean ASD errors with standard deviations for the different contouring strategies tested on the volunteers' real X-ray dataset.

	Volunteer 1	**Volunteer 2**	**Volunteer 3**
not mapped	2.06 ± 1.87 mm	1.42 ± 1.19 mm	1.45 ± 1.15 mm
mapped	1.84 ± 1.99 mm	1.39 ± 1.19 mm	1.29 ± 1.19 mm

We noticed that acquisitions on volunteers were made by radiographers not sufficiently informed on the procedure – resulting in X-ray images acquired without strictly following the provided guidelines, mainly concerning the importance of not moving the subject between the two shots. This may explain the inferior results obtained with respect to the phantom. Indeed, phantom bones are fully static between shots, which convinces us of the potential of the method on real patients by better complying with the acquisition protocol.

4 Conclusion

Under optimal calibration conditions and with precise contours, our method has demonstrated a reconstruction accuracy (ASD 1.02±0.89 mm) comparable or even superior to state-of-the-art methods. Methods reporting accurate results were either tested on synthetic results [9] or dry bones [7], [9], [12], [26], in perfect calibration setup [7], [9], or for the anatomically simpler distal femur [8], [15]. Yu et al. 2016 [9] reported an ASD error of 0.9 mm on synthetic proximal femurs using manual contouring on two fluoroscopy images, but for a database of 40 patients. When switching to real X-ray, in the case of simpler dry femur bone acquired with a C-arm greatly easing the calibration, their error increased to 1.2 mm. Our experiments carried out on a large database of pathological cases support the robustness of the method and its ability to successfully reconstruct complex cases.

To achieve accurate results on clinically interesting cases – in opposition to dry bones for example – the manual segmentation of a pair of 2D mapped contours do not seem a price too high to pay. With an appropriate ergonomic tool, such a task would be less tedious and could replace semi-automatic segmentation on CT scans used today for patient-specific THA planning – benefiting the patient's health and the health costs. However, aware of the importance of automatic tools in the clinical context, we have investigated a DL method for the automatic extraction of AP contours in DRRs with encouraging results (1.68±1.57 mm). The extensive contour analysis has proven their usefulness in achieving accurate results, and their automation has been demonstrated on DRRs with results, albeit not as good, but already usable. The reconstruction is also fast – with a runtime below 30 sec (including 1.8 sec for DL segmentation) – and produces ready-to-use 3D models (e.g., anatomical markers for surgical planning can be predefined on the template models and be immediately available on the reconstructed structures). We particularly envision future work in the automatic and accurate extraction of mapped contours and landmarks from real radiographs albeit the collection of lateral views, less common in clinical practice, may be an interesting yet challenging problem in the context of data hungry algorithms such as deep learning approaches.

Acknowledgement. This work was supported by the Swiss CTI project MyPlanner (no. 25258.1). Authors would like to thank E. Ambrosetti, A. Al-Musibli, L. Assassi and B. Lokaj at the Geneva School of Health Sciences and M. Bernardoni, M. Parravicini and D. Ascani at Medacta International SA.

References

[1] N. Sarkalkan, H. Weinans, and A. A. Zadpoor, "Statistical shape and appearance models of bones," *Bone*, vol. 60, pp. 129–140, Mar. 2014, doi: 10.1016/j.bone.2013.12.006.

[2] P. Gamage, S. Q. Xie, P. Delmas, and W. L. Xu, "Diagnostic radiograph based 3D bone reconstruction framework: Application to the femur," *Computerized Medical Imaging and Graphics*, vol. 35, no. 6, pp. 427–437, Sep. 2011, doi: 10.1016/j.compmedimag.2010.09.008.

[3] P. E. Galibarov, P. J. Prendergast, and A. B. Lennon, "A method to reconstruct patient-specific proximal femur surface models from planar pre-operative radiographs," *Medical Engineering & Physics*, vol. 32, no. 10, pp. 1180–1188, Dec. 2010, doi: 10.1016/j.medengphy.2010.08.009.

[4] P. Markelj, D. Tomaževič, B. Likar, and F. Pernuš, "A review of 3D/2D registration methods for image-guided interventions," *Medical Image Analysis*, vol. 16, no. 3, pp. 642–661, Apr. 2012, doi: 10.1016/j.media.2010.03.005.

[5] C. J. F. Reyneke, M. Lüthi, V. Burdin, T. S. Douglas, T. Vetter, and T. E. M. Mutsvangwa, "Review of 2-D/3-D Reconstruction Using Statistical Shape and Intensity Models and X-Ray Image Synthesis: Toward a Unified Framework," *IEEE Reviews in Biomedical Engineering*, vol. 12, pp. 269–286, 2019, doi: 10.1109/RBME.2018.2876450.

[6] V. Karade and B. Ravi, "3D femur model reconstruction from biplane X-ray images: a novel method based on Laplacian surface deformation," *Int J CARS*, vol. 10, no. 4, pp. 473–485, Apr. 2015, doi: 10.1007/s11548-014-1097-6.

[7] G. Zheng and W. Yu, "Chapter 12 - Statistical Shape and Deformation Models Based 2D–3D Reconstruction," in *Statistical Shape and Deformation Analysis*, G. Zheng, S. Li, and G. Székely, Eds. Academic Press, 2017, pp. 329–349.

[8] O. Klima, P. Kleparnik, M. Spanel, and P. Zemcik, "Intensity-based femoral atlas 2D/3D registration using Levenberg-Marquardt optimisation," in *Medical Imaging 2016: Biomedical Applications in Molecular, Structural, and Functional Imaging*, Mar. 2016, vol. 9788, p. 97880F, doi: 10.1117/12.2216529.

[9] W. Yu, C. Chu, M. Tannast, and G. Zheng, "Fully automatic reconstruction of personalized 3D volumes of the proximal femur from 2D X-ray images," *Int J CARS*, vol. 11, no. 9, pp. 1673–1685, Sep. 2016, doi: 10.1007/s11548-016-1400-9.

[10] N. Baka *et al.*, "2D–3D shape reconstruction of the distal femur from stereo X-ray imaging using statistical shape models," *Medical Image Analysis*, vol. 15, no. 6, pp. 840–850, Dec. 2011, doi: 10.1016/j.media.2011.04.001.

[11] G. Zheng, "Personalized X-Ray Reconstruction of the Proximal Femur via Intensity-Based Non-rigid 2D-3D Registration," in *Medical Image Computing and Computer-Assisted Intervention – MICCAI 2011*, Berlin, Heidelberg, 2011, pp. 598–606, doi: 10.1007/978-3-642-23629-7_73.

[12] H. Boussaid, S. Kadoury, I. Kokkinos, J.-Y. Lazennec, G. Zheng, and N. Paragios, "3D Model-based Reconstruction of the Proximal Femur from Low-dose Biplanar X-Ray Images," in *The 22nd British Machine Vision Conference - BMVC 2011*, Dundee, United Kingdom, Aug. 2011, pp. 1–10, doi: 10.5244/C.25.35.

[13] P. Cerveri, C. Sacco, G. Olgiati, A. Manzotti, and G. Baroni, "2D/3D reconstruction of the distal femur using statistical shape models addressing personalized surgical instruments in knee arthroplasty: A feasibility analysis," *The International Journal of Medical Robotics and Computer Assisted Surgery*, vol. 13, no. 4, p. e1823, 2017, doi: https://doi.org/10.1002/rcs.1823.
[14] K. Youn, M. S. Park, and J. Lee, "Iterative approach for 3D reconstruction of the femur from un-calibrated 2D radiographic images," *Med Eng Phys*, vol. 50, pp. 89–95, Dec. 2017, doi: 10.1016/j.medengphy.2017.08.016.
[15] J. Wu and M. R. Mahfouz, "Reconstruction of knee anatomy from single-plane fluoroscopic x-ray based on a nonlinear statistical shape model," *JMI*, vol. 8, no. 1, p. 016001, Jan. 2021, doi: 10.1117/1.JMI.8.1.016001.
[16] M. R. Mahfouz, W. A. Hoff, R. D. Komistek, and D. A. Dennis, "Effect of segmentation errors on 3D-to-2D registration of implant models in X-ray images," *Journal of Biomechanics*, vol. 38, no. 2, pp. 229–239, Feb. 2005, doi: 10.1016/j.jbiomech.2004.02.025.
[17] R. Grupp *et al.*, "Automatic Annotation of Hip Anatomy in Fluoroscopy for Robust and Efficient 2D/3D Registration," *arXiv:1911.07042 [cs, eess]*, Mar. 2020, doi: 10.1007/s11548-020-02162-7.
[18] Y. Kasten, D. Doktofsky, and I. Kovler, "End-To-End Convolutional Neural Network for 3D Reconstruction of Knee Bones from Bi-planar X-Ray Images," in *Machine Learning for Medical Image Reconstruction*, Cham, 2020, pp. 123–133, doi: 10.1007/978-3-030-61598-7_12.
[19] H. Livyatan, Z. Yaniv, and L. Joskowicz, "Gradient-based 2-D/3-D rigid registration of fluoroscopic X-ray to CT," *IEEE Transactions on Medical Imaging*, vol. 22, no. 11, pp. 1395–1406, Nov. 2003, doi: 10.1109/TMI.2003.819288.
[20] D. Damopoulos *et al.*, "Segmentation of the proximal femur in radial MR scans using a random forest classifier and deformable model registration," *Int J Comput Assist Radiol Surg*, vol. 14, no. 3, pp. 545–561, Mar. 2019, doi: 10.1007/s11548-018-1899-z.
[21] Z. Zhou, M. M. R. Siddiquee, N. Tajbakhsh, and J. Liang, "UNet++: Redesigning Skip Connections to Exploit Multiscale Features in Image Segmentation," *IEEE Trans. Med. Imaging*, vol. 39, no. 6, pp. 1856–1867, Jun. 2020, doi: 10.1109/TMI.2019.2959609.
[22] I. Radosavovic, R. P. Kosaraju, R. Girshick, K. He, and P. Dollar, "Designing Network Design Spaces," in *2020 IEEE/CVF Conference on Computer Vision and Pattern Recognition (CVPR)*, Seattle, WA, USA, Jun. 2020, pp. 10425–10433, doi: 10.1109/CVPR42600.2020.01044.
[23] S. Benameur, M. Mignotte, S. Parent, H. Labelle, W. Skalli, and J. de Guise, "3D/2D registration and segmentation of scoliotic vertebrae using statistical models," *Computerized Medical Imaging and Graphics*, vol. 27, no. 5, pp. 321–337, Sep. 2003, doi: 10.1016/S0895-6111(03)00019-3.
[24] M. Unberath *et al.*, "DeepDRR – A Catalyst for Machine Learning in Fluoroscopy-Guided Procedures," in *Medical Image Computing and Computer Assisted Intervention – MICCAI 2018*, Cham, 2018, vol. 11073, pp. 98–106, doi: 10.1007/978-3-030-00937-3_12.
[25] R. Hataya, J. Zdenek, K. Yoshizoe, and H. Nakayama, "Faster AutoAugment: Learning Augmentation Strategies Using Backpropagation," in *Computer Vision – ECCV 2020*, Cham, 2020, vol. 12370, pp. 1–16, doi: 10.1007/978-3-030-58595-2_1.
[26] R. Kurazume *et al.*, "3D reconstruction of a femoral shape using a parametric model and two 2D fluoroscopic images," *Computer Vision and Image Understanding*, vol. 113, no. 2, pp. 202–211, Feb. 2009, doi: 10.1016/j.cviu.2008.08.012.